Influence of Microstructure on Symmetry Determination of Piezoceramics

M. Hinterstein[1,2], H.E. Mgbemere[3], M. Hoelzel[4], W. Rheinheimer[1], E. Adabifiroozjaei[2], P. Koshy[2], C.C. Sorrell[2] and M. Hoffman[2]

[1] Institute for Applied Materials, Karlsruhe Institute of Technology, 76131 Karlsruhe, Germany
[2] School of Materials Science and Engineering, UNSW Sydney, Sydney, Australia
[3] Department of Metallurgical and Materials Engineering, University of Lagos, Akoka, Lagos, Nigeria
[4] Heinz Maier-Leibnitz Zentrum, Technische Universität München, Garching, Germany

The origin of the complex reflection splitting in potassium sodium niobate, doped with lithium and manganese, was investigated using temperature-dependent high-resolution X-ray and neutron diffraction as well as electron probe microanalysis and scanning electron microscopy. Two structural models were developed from the diffraction data. A single-phase monoclinic *Pm* model is known from literature and is able to reproduce perfectly the diffraction patterns. However, a model with phase coexistence of two classical orthorhombic *Amm*2 phases also can reproduce the diffraction data with equal accuracy. Scanning electron microscopy in combination with electron probe microanalysis revealed segregation of the A-site substituents potassium and sodium. This favours the model with phase coexistence and demonstrates the need for comprehensive analyses with complementary methods to cover a broad range of length scales as well as to assess both average and local structure.

1. Introduction

The influence of the microstructure on diffraction patterns is a widely discussed issue in materials science. For piezoceramics in particular, not only the grain morphology but also the microstructure of the grains themselves play crucial roles. The more common solid solutions, such as lead zirconate titanate (PZT) [1] and barium titanate (BT) [2], exhibit complex domain structures, especially in the vicinity of the phase boundaries [3–5]. These complex structures cause anisotropic reflection broadening since the domain walls interrupt the ideal structure and prevent the development of a homogeneous crystal structure throughout the grains [6,7].

With the improvement of diffraction techniques, the phase diagrams of many piezoelectric systems have been revised [8–16]. While most systems can be characterised in terms of rhombohedral, orthorhombic, or tetragonal phases, high-resolution measurements have revealed the existence of monoclinic phases [17–19]. For lead zirconate titanate (PZT), a monoclinic *Cm* phase has been proposed at the phase boundary between the tetragonal *P*4*mm* and the rhombohedral *R*3*m* phases above room temperature [17]. Below room temperature the R3m phase transforms to *R*3*c* with oxygen octahedral tilting. This low-temperature modification subsequently was found to exhibit monoclinic *Cc* symmetry instead of rhombohedral *R*3*c* symmetry [20].

In the lead-free bismuth sodium titanate (BNT) system, the rhombohedral *R*3*c* phase was reported to be of monoclinic *Cc* symmetry [21] and this was confirmed with single-crystal diffraction [18]. A similar discussion remains pending for the potassium sodium niobate (KNN) system. For the composition $K_{0.5}Na_{0.5}NbO_3$, there remains uncertainty whether the structure is orthorhombic *Amm*2 [22] or monoclinic *Pm* [13]. However, this represents a special case since *Amm*2 does not describe a primitive cell; it contains two formula units and two of the axes are primitive $[110]_C$ directions. Different lattice parameters for these two axes result in a rhombic distortion of the (001) plane, giving the primitive cell monoclinic symmetry [19]. In contrast, the *Pm* structure is set up as a primitive cell, resulting in the possibility of having three different lengths for the primitive axes [19].

The rationale for the preceding cases often is based on the agreement factors for Rietveld refinements [14–16,21,23,24]. Since the complex real structure generates anisotropic reflection broadening, the increased number of reflections representing the monoclinic phases assists in modelling the measured profiles. Only a few studies have provided evidence of lower symmetry by clear reflection splitting [17–19].

For undoped PZT, a clear additional reflection has suggested a monoclinic modification [17]. However, other studies have attempted to explain this observation by either coherent scattering of the nanodomains or phase coexistence [25]. It is only with BNT that a single-crystal diffraction experiment has demonstrated unambiguously the existence of monoclinic reflection splitting [18]. Further, only with powder diffraction data has pronounced reflection broadening been observed [21].

All high-performance piezoceramics are located near phase boundaries in systems exhibiting solid solubility. The best known system is PZT with B-site substitution of zirconium by titanium [1]. Both BNT and KNN are A-site substituted while, for BT, a typical combination includes A- and B-site substitutions with Ca and Zr, respectively, to form the complex system $(1\text{-}x)Ba(Zr_yTi_{1\text{-}y})O_{3\text{-}x}(Ba_zCa_{1\text{-}z})TiO_3$ [10]. Grinberg *et al.* [26] showed by density functional theory (DFT) calculations that the distribution of the substituted species influences the local structure of the material.

The present study demonstrates the challenges of structure determination for KNN-based functional piezoceramics. The complex microstructure results in diffraction patterns that can be interpreted in terms of low symmetry or phase coexistence. Based on agreement factors alone, neither of the models can be considered as definitive. However, a supported conclusion can be drawn using a combination of microstructural and elemental analytical methods.

2. Experimental

KNN-$Li_2Mn[(K_{0.48}Na_{0.48}Li_{0.04})(Nb_{0.98}Mn_{0.02})O_3]$ was produced from K_2CO_3, Na_2CO_3, Li_2CO_3 (all 99 wt%), Nb_2O_5 (99.9%) (Chempur Feinchemikalien und Forschungs GmbH, Karlsruhe, Germany), and MnO_2 (95%) (Merck Chemicals Darmstadt, Germany). The powders were dried at 220°C for 4 h in order to remove moisture. Stoichiometric amounts of the starting oxides were batched but 2 mol% excess of the carbonates were used in order to compensate for losses during sintering [26,27]. The powders were mixed and milled using an attrition mill (NETZSCH-Feinmahltechnik GmbH) operating at 500 rpm for 2 h with ethanol as medium and 3 mm yttria-stabilised zirconia balls as grinding media. The solvent (ethanol) was removed using a rotary evaporator (Rotavapor R-100 BÜCHI Labortechnik AG, Flawil, Switzerland), after which they were placed in alumina crucibles and calcined in a tube furnace at 850°C for 4 h at a heating rate of 3°C/min, followed by cooling at 10°C/min. Following calcining, the attrition milling process was repeated in order to homogenise the powders and to reduce the average particle size of the powders to <1 µm. The powders then were cold isostatically pressed (wet-bag method) at 300 MPa for 2 min. The samples were placed on alumina supports and sintered in air at 1050°C for 1 h, using a heating rate of 2°C/min and a cooling rate of 10°C/min.

High-resolution synchrotron X-ray powder diffraction data were obtained using flat-plate transmission geometry at the B2 beamline at Deutsches Elektronen-Synchrotron (DESY) in Hamburg, Germany [28] using the Analyser Crystal Detector at a beam energy of 18 keV (λ = 0.6881 Å) with a step width of 0.002° 2θ. High-resolution neutron powder diffraction data were obtained from a sintered cylindrical sample of ~400 mm³ using the SPODI beamline at the Maier Leibnitz-Zentrum in Garching, Germany [29]. This beamline operates at a wavelength λ = 1.548 Å using a bank of eighty position-sensitive ^{3}He detectors that cover a 160° scattering range. High-temperature measurements were performed *in situ* in a high-temperature furnace in the range 300-500 K. Since the furnace elements consisted of niobium, it was necessary to heat under vacuum (10^{-5} mbar) in order to prevent oxidation.

Rietveld refinement was performed using the *Fullprof* Software package [30]. Refinement of phases with rhombohedral (*R*3*c*), monoclinic (*Pm*), orthorhombic (*Amm*2), tetragonal (*P*4*mm*), and cubic ($Pm\overline{3}m$) symmetry was implemented in the structure model. The background was refined using linear interpolation between points from the regions where no reflections contributed to the intensities. The profile function was described using the Thompson-Cox-Hastings pseudo-Voigt model [31]. The lattice parameters, atomic positions, and isotropic atomic displacement parameters B_{iso} for all suitable elements were refined. The integral breadth was calculated after subtraction of instrumental broadening and the implementation of a model for anisotropic peak broadening, developed by Stephens [32]. This model considers the case of an anisotropic distribution of strain, in which the diffraction peak width increases in proportion to the diffraction order. The instrumental broadening was determined by a Rietveld fit of a high-resolution measurement recorded at ambient temperature of the standard reference material LaB6 (SRM 660a, National Institute of Standards, NIST) for X-ray measurements and Si (SRM 640c, National Institute of Standards, NIST) for neutron measurements.

The elemental distributions were analysed by electron probe microanalysis (EPMA; JEOL JXA-8500F, Tokyo, Japan) equipped with four wavelength dispersive spectrometers (WDS) that were individually optimised for the detection of the different elements. Quantitative microstructural analysis of the EPMA scans was performed using ImageJ [33].

3. Results

3.1. Powder diffraction

The authors recently published a report of doped KNN that showed clear reflection splitting [19]. The data were modelled unambiguously with a monoclinic *Pm* structure, the evidence for which is shown in Figure 1a). There also is direct evidence of reflection splitting from the monoclinic angle, *e.g.*, for the 110_C reflection (arrow in Figure 1a) inset I)), and the three different axial lengths of the primitive unit cell, *e.g.*, for the 200_C reflection (Figure 1a), inset II). Although the insets of Figure 1a) indicate imperfect agreement between the measured data and the fit, closer examination suggests that the cause is the complicated profile and anisotropic reflection broadening due to microstrain. Analysis of the reflection widths by Rietveld refinement confirms this assessment and reveals the strongest anisotropy for the 200_C reflection, with microstrains of 0.104% for the 020_M reflection, 0.238% for the 002_M reflection, and 0.333% for the 200_M reflection. These anisotropic microstrains are well known to originate from lattice mismatch at domain walls [34,35].

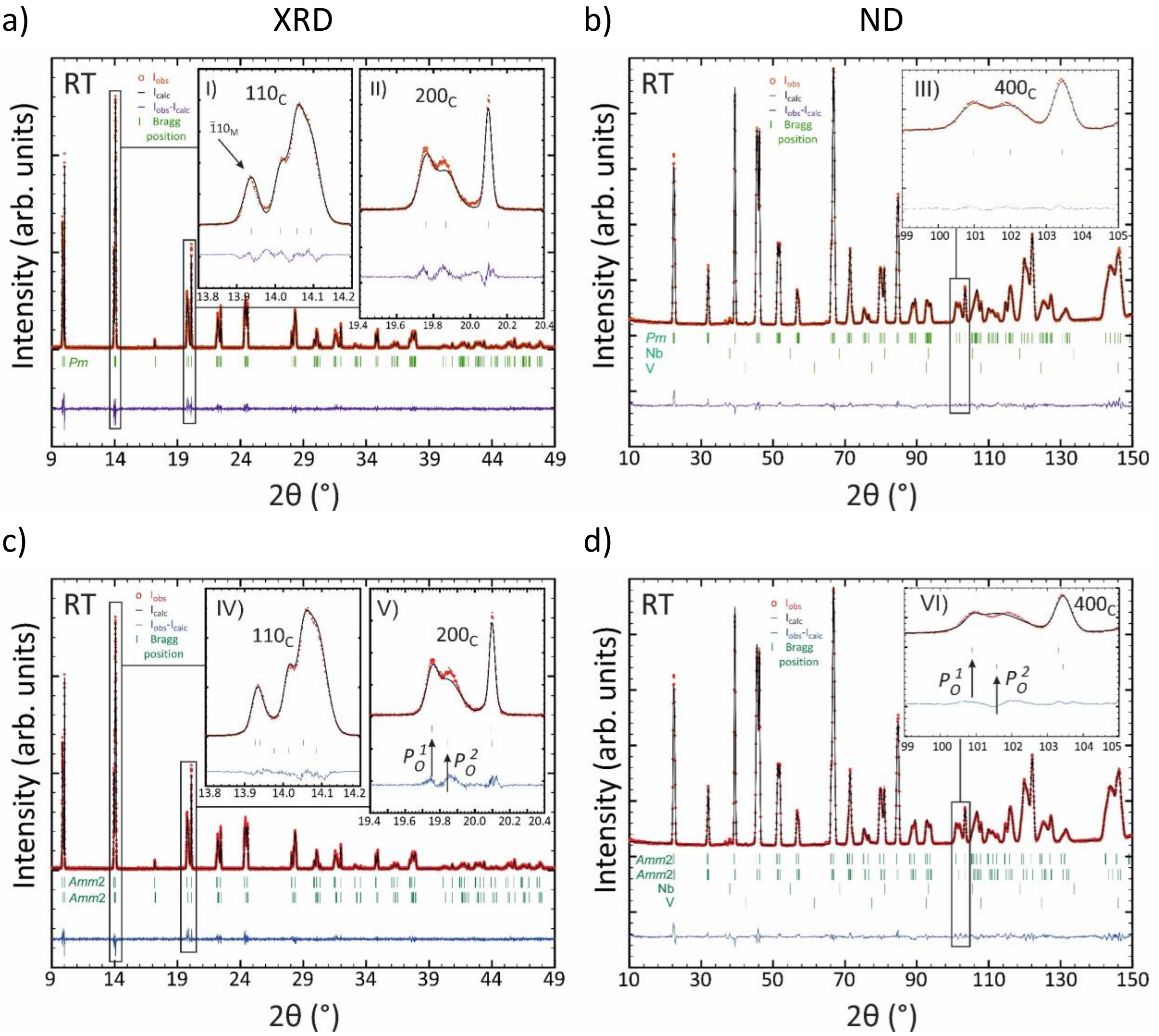

Figure 1: Rietveld refinement of a) & c) high-resolution synchrotron X-ray diffraction data and b) & d) high-resolution neutron diffraction data for KNN-Li2Mn. The red dots show the measurements, the black curves indicate the calculated diffraction patterns, and the blue curves show the difference of fit. The green vertical lines indicate the positions of the Bragg reflections. a) & b) show the fit for a single-phase Pm structure model. Inset I) shows the 110C reflection with clear splitting into the 110M and the $\bar{1}$11M reflection (arrow) due to the monoclinic angle. The reflection clearly is comprised of four reflections instead of three when space group *Amm*2 is used. Inset II) depicts the 200C reflection with clear threefold splitting due to the three different monoclinic primitive axes. Inset III) shows clear threefold splitting (101°, 102° and 103.5° 2θ) of the 400C reflection. c) & d) show a fit for a structure model with two phases of space group *Amm*2. Inset IV) shows fourfold splitting of the 110C reflection; inset V) shows threefold splitting of the 200C reflection; inset VI) shows threefold splitting of the 400C reflection. As the niobium heat shield gives rise to a clearly visible 110 reflection at about 38.5° and the vanadium sample container gives rise to a 110 reflection at about 42.5°, these phases are included in the fitting.

Further analysis by high-resolution neutron diffraction, shown in Figure 1b), depicts the Rietveld refinement with the same structure model used for the high-resolution synchrotron X-ray diffraction data. The threefold splitting of the 00*l* reflections can be observed and is modelled adequately by the fit (Figure 1b), inset III). The authors have published this structure model, albeit with less detail, for the same material [19]. Other studies reached the same conclusion for similar KNN compositions, although without clear reflection splitting [8,13,36–39]. The present work appears to resolve such clear reflection splitting for the first time, which is attributed to the extraordinary angular resolution of the X-ray and neutron diffraction data.

Since KNN-Li2Mn showed the features of *Pm* symmetry clearly and distinctively, its temperature-dependence was investigated in further detail using neutron diffraction. A previous X-ray study suggested the existence of phase transformations to tetragonal at ~150°C and to a paraelectric cubic phase at ~450°C [19]. Therefore, data were obtained for the material at temperatures within the tetragonal range (250°C, Figure 2a)) and above the Curie temperature (500°C, Figure 2b)).

Surprisingly, it was not possible to refine the data above the Curie temperature using a cubic space group. All higher indexed reflections show clear splitting. The most appropriate method of describing the structure is with the use of two identical cubic phases of different lattice parameters. Figure 2b) shows the Rietveld refinement at 500°C with two cubic phases P_C^1 (a_1 = 3.98997(7) Å) and P_C^2 (a_2 = 3.98337(10) Å). The distinct splitting of the highest indexed reflection 422_C (arrows P_C^1 and P_C^2 in inset in Figure 2b)) clearly shows that the material is comprised of more than a single-phase.

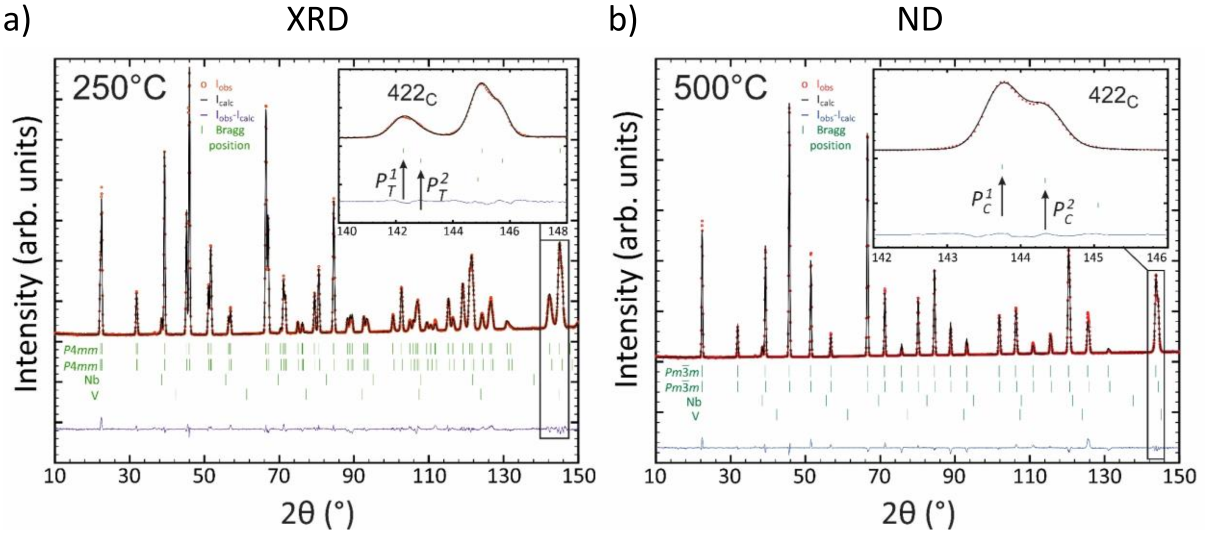

Figure 2: Rietveld refinement of high-resolution neutron diffraction data of KNN-Li2Mn at a) 250°C and b) 500°C. The red dots show the measurements, the black curves indicate the calculated diffraction patterns, and the blue curves show the difference of fit. The green vertical lines indicate the positions of the Bragg reflections. The insets show the clear splitting of the 422_C reflection.
As the niobium heat shield gives rise to a clearly visible (110) reflection at about 38.5° and the vanadium sample container gives rise to a 110 reflection at about 42.5°, these phases are included in the fitting.

Closer examination of the results for the tetragonal stability region at 250°C shows that the measured data can be described only by the existence of two phases as well (P_T^1 and P_T^2, Figure 2a)). In this case, two tetragonal *P*4*mm* phases with different lattice parameters allow adequate modelling of the observed data. In light of these results for the measurements at 250°C and 500°C, the measurements at room temperature require reassessment. The literature [8,19] and earlier observations suggest that the phase transformation sequence in KNN-Li2Mn should be:

$$Amm2 \xrightarrow{150°\mathrm{C}} P4mm \xrightarrow{450°\mathrm{C}} Pm\bar{3}m$$

Careful revision of the refinements reveals that the room-temperature data can be modelled with two similar phases as well: P_O^1 and P_O^2. Accordingly, the monoclinic phase is not necessarily needed to refine the structure.

A use of two *Amm*2 phases also results in good agreement between fit and observations for both high-resolution synchrotron and neutron diffraction data ((P_O^1 and P_O^2, Figure 1 c) & d)). While the refinement with the synchrotron data (Figure 1c)) appears similar to that using *Pm* (Figure 1a)), the model is not capable of reproducing the threefold splitting of the 400_{C} reflection with neutron diffraction (Figure 1d)), resulting in a slightly inferior fit. Since orthorhombic phases exhibit fewer degrees of freedom than monoclinic phases, the fit of the pronounced anisotropic reflection broadening is limited.

Table 1 lists details of the refinements for the different temperatures and structure models. The *R*-values and χ^2 for the synchrotron refinements at room temperature reveal that the two-phase model is better, with sixty-three fit parameters compared to forty-three for the single-phase model. Since this is a significant increase of the number of degrees of freedom, this result is not surprising. The agreement factors for neutron diffraction indicate an inferior fit for the two-phase model in spite of the significant increase in the number of degrees of freedom. With increasing temperature, the quality of the neutron refinements decreases together with the number of fit parameters.

Table 1: Details of the Rietveld refinements for the different temperatures and structure models. The number of refined parameters is given for every discussed structure model, temperature and measurement. Goodness of fit parameter (χ^2), profile (R_p) and weighted profile R-factor (R_{wp}) are given as well.

Temperature	**Room Temperature**				**250°C**	**500°C**
Source	**XRD**		**ND**		**ND**	**ND**
Phases	*Pm*	*Amm*2 + *Amm*2	*Pm*	*Amm*2 + *Amm*2	*P*4*mm* + *P*4*mm*	*Pm*3*m* + *Pm*3*m*
No. of Parameters	43	63	49	66	39	27
R_P	15.10	15.00	4.81	5.65	6.46	9.20
R_{WP}	18.40	17.70	5.01	5.82	6.98	9.81
χ^2	1.519	1.355	4.281	5.389	7.721	14.790

Considering only the agreement factors and the appearance of the fits, single-phase *Pm* appears to be the correct structure model. Further, given the common symmetry evolutions with temperature, it is highly unlikely that coexisting phases of high symmetry transform to a single low-symmetry phase at lower temperatures. Usually, symmetry increases with increasing temperature owing to the Gibbs free energy dependence. In principle, there are several possible scenarios in which coexisting phases transform to a single-phase with decreasing temperature. Superlattices, spinodal decompositions, and subsolidus miscibility gaps are such cases.

Although the coexistence of two orthorhombic *Amm*2 phases at room temperature seems more likely, it is clear that it is not possible to judge a structure model from fit parameters by implication [40]. In fact, careful assessment of the microstructure by complementary techniques, such as electron microscopy, followed by conclusions based on physically reasonable arguments, would be advantageous.

3.2. Electron microscopy

In order to determine the origin of this phase coexistence and to correlate the crystallography with the microstructure, the local microstructure was investigated using electron probe microanalysis with wavelength dispersive spectroscopy (EPMA-WDS). Figure 3 and 4 illustrate the results of two scans of the same area using different sample currents and dwell times.

When scanned at a lower sample current of 40 nA, a bimodal distribution of the A-site cations was clearly evident. When the sample current was increased to 80 nA, as shown in Figure 3, the bimodal distribution of A-site cations was even more pronounced, indicating this to be a bulk phenomenon rather than a surface effect or an outcome of thermal etching. While potassium is enriched at the grain boundaries, sodium has a higher concentration in the bulk of the grains. The distribution map also exhibits regions where neither of the two elements can be found. These correspond to pores in the sample, which appear as either black holes in the SEM image or dark grey areas between the grains.

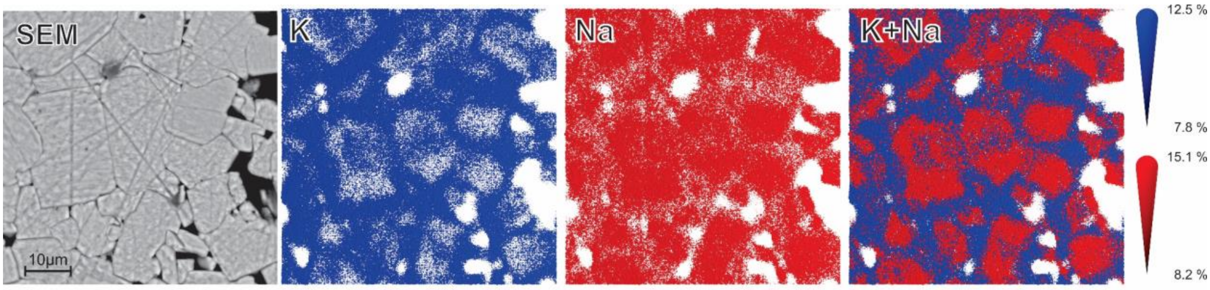

Figure 3: EPMA-WDS scans of a 60 x 60 µm^2 area with elemental mapping of K and Na as well as the corresponding SEM image. At an accelerating voltage of 20 kV, the sample current was adjusted to 80 nA, with a dwell time of 25 ms per point and a step width of 0.2 µm for the mapping. Individual scan points are represented by spheres with diameters proportional to the mol% of the elements.

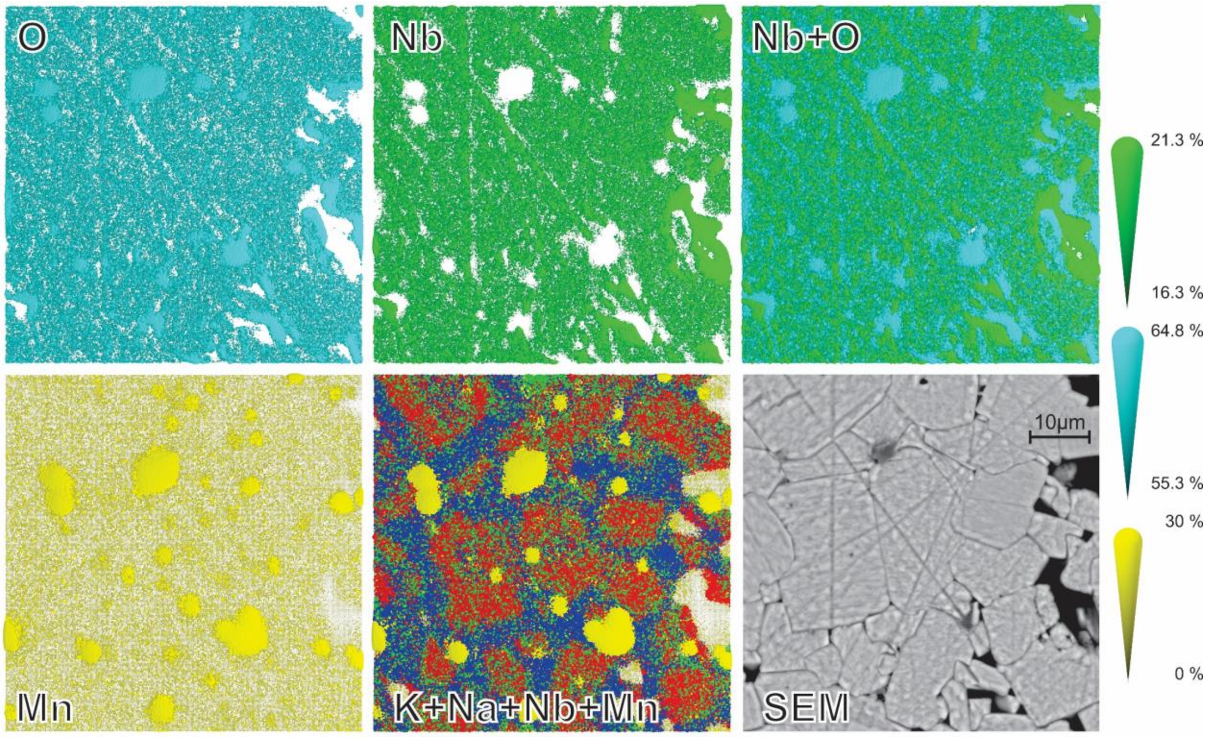

Figure 4: EPMA-WDS scans of a 60 x 60 µm^2 area with elemental mapping of O, Nb, and Mn together with K and Na as well as the corresponding SEM image. At an accelerating voltage of 20 kV, the sample current was adjusted to 80nA, with a dwell time of 25 ms per point and a step width of 0.2 µm for the mapping. Individual scan points are represented by spheres with diameters proportional to the mol% of the elements.

For further clarity, a second scan at a higher sample current and shorter dwell time was obtained in order to map oxygen and manganese (Figure 4). The results show that the sample exhibits a continuous oxygen matrix and discrete particles of manganese oxide. It is clear that the manganese content was higher than the manganese solubility. Consequently, the manganese doping is distributed uniformly throughout the matrix grains and shows no correlation with the A-site distribution.

The same areas depicted in Figure 3 Figure 4 were scanned (thirty points) at a sample current of 22 nA and a dwell time of 20 s in order to compare spatial distributions and counting statistics. Table 2 summarises the analysis of the two mapping scans at the selected points and compares them with the results from the Rietveld refinement and image analyses for the Na-rich and K-rich distributions (40 nA, 40 ms) from Figure 3.

Table 2: EPMA-WDS results*.

i, t	**22 nA, 20 s**		**40 nA, 40 ms**		**80 nA, 25 ms**		**Image Analyses**		**Rietveld Fit**	
Element	**Na**	**K**	**Na**	**K**	**Na**	**K**	P_O^1 **(Na-rich)**	P_O^2 **(K-rich)**	P_O^1 **(Na-rich)**	P_O^2 **(K-rich)**
x (mol%)	9.78	9.62	11.61	10.15	10.83	9.31				
FWHM (%)	-	-	1.72	1.18	1.37	1.05				
Mean x (mol%)	9.70		10.46		9.94					
Mean w(%)	-		1.32		1.46					
Fraction (%)	50.41	49.59	55.53	48.55	54.46	46.82	52.78	47.21	52.5(5)	47.5(5)
FWHM (%)	-	-	8.20	5.65	6.89	5.29				

*The values measured at 22 nA were obtained from thirty selected points and summed. The values measured at 40 nA and 80 nA are total sums for scans over the same 60 x 60µm^2 area with a step width of 0.2 µm. Image analyses were performed on the Na-rich and K-rich distributions (40 nA, 40 ms) using the data in Figure 3.

The EPMA-WDS results clearly show that Na and K are segregated into different regions within the microstructure. Na is mostly present within the grains and K is predominantly located at the grain boundaries. The image analyses and the results from Rietveld refinement for the two orthorhombic phases O_1 and O_2 show excellent agreement, strengthening the concept of coexistence of two similar phases with different Na/K ratios over the entire temperature range.

4. Discussion

In summary, the EPMA-WDS, X-ray diffraction, and neutron diffraction data show segregation at the grain boundaries, resulting in two different chemical compositions (Na/K) at the grain boundaries and in the core of the grains. A similar core-shell microstructure has been reported before for KNN [41,42], doped barium titanate [43,44], and barium strontium titanate [45]. Many other important perovskite materials potentially show similar behaviour as they are either doped or have A- or B-site substitution (*e.g.*, PZT [46], BT [43,44], ST [47], BCT-BZT [48], BNT [49], BNT-BT [50], BNT-BT-KNN [51], BNT-ST [45,52,53], KNN [41,54], and BSCF [55]). Accordingly, this behaviour and its origin are of considerable interest.

In principle, segregation can have several different causes but its origin lies in the kinetics or thermodynamics. Segregation from kinetic effects could arise during calcination. For example, if the solid-state reaction kinetics of Na and K with Nb_2O_5 differ, the concentrations of Na and K would be inhomogeneous, so the species with lower diffusivity would have a lower concentration in the centre of the particles. This phenomenon has been reported for BST [45] and BT [43]. However, the resulting core-shell distribution is limited spatially to the initial powder particle size, which was <1 µm. Since the microstructures shown in Figure 3 and Figure 4 are very coarse, it is unlikely that segregation from calcination or sintering would be sustained during the extensive grain growth, so kinetic issues during calcination are unlikely.

In contrast, segregation from kinetic effects during sintering are quite probable owing to volatilisation. The volatilisation rate of Na can be concluded to be greater than that of K owing to the observation of the formation of K-rich surface layers [41,42,56]. The microstructure shown in Figure 3 and Figure 4 support the view that segregation occurred during the sintering process. It also is likely that the extensive grain growth was assisted by the concentration of the alkalis in both the bulk and at the surfaces since these ions are well known as high-diffusivity fluxes for oxides.

Thermodynamically, segregation may arise from the existence of charged boundaries and the formation of adjacent space charge [57–59]. However, the typical width of concentration gradients due to space charge is in the range of tens of nm while that observed in Figure 3 is of the order of several microns. Another source of thermodynamic segregation has been designated as a *complexion*, where a thin segregated (adsorption) film at the interfaces may form due to interfacial energy minimisation [60–62]. However, since these films usually are atomically disordered and have a width of only a few nanometres, this phenomenon is unlikely.

Finally, a plausible kinetic and thermodynamic basis for the observed segregation could be the miscibility gap that is observed in some systems containing Na and K, including NaCl-KCl [63,64], $NaAlSi_3O_8$-$KAlSi_3O_8$ [65], $NaNO_3$-KNO_3 [66] and $Na_3K(AlSiO_4)_4$–$K_4(AlSiO_4)_4$ [67], although it has not been reported for the $NaNbO_3$-$KNbO_3$ system [68,69]. Such a subsolidus miscibility gap could result in the thermodynamic stability of two different material compositions. That is, a homogenous single-phase solid solution at the sintering temperature would undergo transformation into two solid solution end-members of different compositions upon cooling. These microstructures are indicative of the incomplete phase separation of the Na-rich and K-rich conjugate phases, which would explain both the appearance and evolution of the observed microstructures.

5. Conclusions

The present work shows that local variations in the substituted species distribution can lead to phenomena that can be explained by monoclinic average symmetry as well as phase coexistence of higher symmetry phases. Only a temperature-dependent X-ray and neutron diffraction study in conjunction with precise wavelength dispersive spectroscopy (WDS) elemental analyses are able to demonstrate local differences in concentrations of the substituted species, resulting in a bimodal distribution of concentrations with different crystal structures.

This represents an extreme case of segregation (in the generic sense of this term) on the micron scale. However, while intermediate chemical segregation down to the unit cell level is conceivable, although this would be uncertain as such a scale. Many perovskites and other materials are known to show such segregation at the interfaces, which may be caused by, *inter alia*, charged boundary cores or interfacial stresses. The typical scale of interfacial segregation in these materials at high temperatures is of the order of 10-500 nm [57,60,70].

The present work demonstrates that the use of Rietveld refinement alone can make structure determinations challenging. However, the underlying mechanisms of the extraordinary properties of some functional materials originate not just in their structures but also their complex microstructures. Consequently, knowledge of both features of materials may be essential for the exploitation and development of their functionalities.

Acknowledgements

M. Hinterstein acknowledges funding from the 'Deutsche Forschungsgemeinschaft' (DFG) for the Emmy Noether Research Group HI1867/1-1.

References

[1] B. Jaffe, W. R. Cook, and H. Jaffe, *Piezoelectric Ceramics* (Academic Press, London, 1971).

[2] H. F. Kay and P. Vousden, Philos. Mag. Ser. 7 **40**, 1019 (1949).

[3] K. A. Schoenau, L. A. Schmitt, M. Knapp, H. Fuess, R.-A. Eichel, H. Kungl, and M. J. Hoffmann, Phys. Rev. B **75**, 184117 (2007).

[4] R. Theissmann, L. A. Schmitt, J. Kling, R. Schierholz, K. A. Schoenau, H. Fuess, M. Knapp, H. Kungl, and M. J. Hoffmann, J. Appl. Phys. **102**, 24111 (2007).

[5] P. W. Forsbergh, Phys. Rev. **76**, 1187 (1949).

[6] H. Boysen, J. Phys. Condens. Matter **19**, 275206 (2007).

[7] H. Boysen, Zeitschrift Für Krist. **220**, 726 (2005).

[8] D. W. Baker, P. A. Thomas, N. Zhang, and A. M. Glazer, Appl. Phys. Lett. **95**, 91903 (2009).

[9] D. E. Cox, B. Noheda, G. Shirane, Y. Uesu, K. Fujishiro, and Y. Yamada, Appl. Phys. Lett. **79**, 400 (2001).

[10] D. S. Keeble, F. Benabdallah, P. A. Thomas, M. Maglione, and J. Kreisel, Appl. Phys. Lett. **102**, 92903 (2013).

[11] D. La-Orauttapong, B. Noheda, Z.-G. Ye, P. M. Gehring, J. Toulouse, D. E. Cox, and G. Shirane, Phys. Rev. B **65**, 1 (2002).

[12] N. Zhang, H. Yokota, A. M. Glazer, Z. Ren, D. A. Keen, D. S. Keeble, P. A. Thomas, and Z.-G. Ye, Nat. Commun. **5**, 5231 (2014).

[13] J. Tellier, B. Malic, B. Dkhil, D. Jenko, J. Cilensek, and M. Kosec, Solid State Sci. **11**, 320 (2009).

[14] R. Ranjan, S. K. Mishra, and D. Pandey, J. Appl. Phys. **92**, 3266 (2002).

[15] N. Zhang, H. Yokota, A. M. Glazer, and P. A. Thomas, Acta Crystallogr. B. **67**, 386 (2011).

[16] N. Zhang, H. Yokota, A. M. Glazer, and P. A. Thomas, Acta Crystallogr. Sect. B Struct. Sci. **67**, 461 (2011).

[17] B. Noheda, D. E. Cox, G. Shirane, J. A. Gonzalo, L. E. Cross, and S.-E. Park, Appl. Phys. Lett. **74**, 2059 (1999).

[18] S. Gorfman and P. A. Thomas, J. Appl. Crystallogr. **43**, 1409 (2010).

[19] H. E. Mgbemere, M. Hinterstein, and G. A. Schneider, J. Eur. Ceram. Soc. **32**, 4341 (2012).

[20] S. K. Mishra, D. Pandey, H. Lemmens, and G. Tendeloo, Phys. Rev. B **64**, 54101 (2001).

[21] E. Aksel, J. S. Forrester, J. L. Jones, P. A. Thomas, K. Page, and M. R. Suchomel, Appl. Phys. Lett. **98**, 152901 (2011).

[22] H. E. Mgbemere, M. Hinterstein, and G. A. Schneider, J. Appl. Crystallogr. **44**, 1080 (2011).

[23] D. Pandey and R. Agini, Zeitschrift Für Krist. **218**, 1 (2003).

[24] R. Ranjan, S. K. Mishra, D. Pandey, and B. Kennedy, Phys. Rev. B **65**, 1 (2002).

[25] Y. Wang, Phys. Rev. B **76**, 24108 (2007).

[26] Z. S. Ahn and W. A. Schulze, J. Am. Ceram. Soc. **70**, C18 (1987).

[27] P. Bomlai, P. Wichianrat, S. Muensit, and S. J. Milne, J. Am. Ceram. Soc. **90**, 1650 (2007).

[28] M. Knapp, C. Baehtz, H. Ehrenberg, and H. Fuess, J. Synchrotron Radiat. **11**, 328 (2004).

[29] M. Hoelzel, A. Senyshyn, N. Juenke, H. Boysen, W. Schmahl, and H. Fuess, Nucl. Instruments Methods Phys. Res. Sect. A Accel. Spectrometers, Detect. Assoc. Equip. **667**, 32 (2012).

[30] J. Rodríguez-Carvajal, Phys. B Condens. Matter **192**, 55 (1993).

[31] P. Thompson, D. E. Cox, and J. B. Hastings, J. Appl. Crystallogr. **20**, 79 (1987).

[32] P. W. Stephens, J. Appl. Crystallogr. **32**, 281 (1999).

[33] C. A. Schneider, W. S. Rasband, and K. W. Eliceiri, Nat. Methods **9**, 671 (2012).

[34] Y.-K. Choi, T. Hoshina, H. Takeda, T. Teranishi, and T. Tsurumi, Appl. Phys. Lett. **97**, 212907 (2010).
[35] J. E. Daniels, J. L. Jones, and T. R. Finlayson, J. Phys. D. Appl. Phys. **39**, 5294 (2006).
[36] A. Bencan, E. Tchernychova, M. Godec, J. Fisher, and M. Kosec, Microsc. Microanal. **15**, 435 (2009).
[37] H. E. Mgbemere, G. A. Schneider, M. Hoelzel, and M. Hinterstein, J. Appl. Crystallogr. **49**, 891 (2016).
[38] Y. Shiratori, A. Magrez, and C. Pithan, J. Eur. Ceram. Soc. **25**, 2075 (2005).
[39] L. Liu, M. Knapp, H. Ehrenberg, L. Fang, L. A. Schmitt, H. Fuess, M. Hoelzel, and M. Hinterstein, J. Appl. Crystallogr. **49**, 574 (2016).
[40] B. H. Toby, Powder Diffr. **21**, 67 (2006).
[41] Y. Zhen and J.-F. Li, J. Am. Ceram. Soc. **90**, 3496 (2007).
[42] Y. Zhen and J.-F. Li, J. Am. Ceram. Soc. **89**, 3669 (2006).
[43] S.-C. Jeon, C.-S. Lee, and S.-J. L. Kang, J. Am. Ceram. Soc. **95**, 2435 (2012).
[44] S.-C. Jeon and S.-J. L. Kang, Appl. Phys. Lett. **102**, 112915 (2013).
[45] J.-S. Kim and S.-J. L. Kang, J. Am. Ceram. Soc. **82**, 1085 (1999).
[46] M. Hammer and M. J. Hoffmann, J. Am. Ceram. Soc. **81**, 3277 (1998).
[47] S.-Y. Chung, B.-K. Lee, and S.-J. L. Kang, J. Am. Ceram. Soc. **81**, 3016 (2005).
[48] Z. Wang, K. Zhao, X. Guo, W. Sun, H. Jiang, X. Han, X. Tao, Z. Cheng, H. Zhao, H. Kimura, G. Yuan, J. Yin, and Z. Liu, J. Mater. Chem. C **1**, 522 (2013).
[49] X. Liu and X. Tan, Adv. Mater. **28**, 574 (2016).
[50] M. Hinterstein, L. A. Schmitt, M. Hoelzel, W. Jo, J. Rödel, H.-J. Kleebe, and M. Hoffman, Appl. Phys. Lett. **106**, 222904 (2015).
[51] L. A. Schmitt and H.-J. Kleebe, Funct. Mater. Lett. **3**, 55 (2010).
[52] J. Koruza, V. Rojas, L. Molina-Luna, U. Kunz, M. Duerrschnabel, H.-J. Kleebe, and M. Acosta, J. Eur. Ceram. Soc. **36**, 1009 (2016).
[53] M. Acosta, L. A. Schmitt, L. Molina-Luna, M. C. Scherrer, M. Brilz, K. G. Webber, M. Deluca, H.-J. Kleebe, J. Rödel, and W. Donner, J. Am. Ceram. Soc. **98**, 3405 (2015).
[54] Y. Wang, D. Damjanovic, N. Klein, E. Hollenstein, and N. Setter, J. Am. Ceram. Soc. **90**, 3485 (2007).
[55] W. Zhou, F. Liang, Z. Shao, J. Chen, and Z. Zhu, Sci. Rep. **1**, 155 (2011).
[56] J. Acker, H. Kungl, R. Schierholz, S. Wagner, R.-A. Eichel, and M. J. Hoffmann, J. Eur. Ceram. Soc. **34**, 4213 (2014).
[57] Y.-M. Chiang and T. Takagi, J. Am. Ceram. Soc. **73**, 3278 (1990).
[58] A. P. Sutton and R. W. Balluffi, *Interfaces in Crystalline Materials* (Clarendon, 1996).
[59] Y. Chiang, D. P. Birnie, and W. D. Kingery, *Physical Ceramics* (J. Wiley, 1997).
[60] W. Rheinheimer and M. J. Hoffmann, Curr. Opin. Solid State Mater. Sci. (2016).
[61] P. R. Cantwell, M. Tang, S. J. Dillon, J. Luo, G. S. Rohrer, and M. P. Harmer, Acta Mater. **62**, 1 (2014).
[62] S. J. Dillon, M. Tang, W. C. Carter, and M. P. Harmer, Acta Mater. **55**, 6208 (2007).
[63] J. B. Thompson and D. R. Waldbaum, Geochim. Cosmochim. Acta **33**, 671 (1969).
[64] B. P. Burton and A. van de Walle, Chem. Geol. **225**, 222 (2006).
[65] R. A. Yund and J. Tullis, *Feldspar Mineralogy: Reviews in Mineralogy: Vol. 2* (Mineralogical Society of America, Chelsea, MI, 1983).
[66] R. S. Roth, J. R. Dennis, and H. McMurdie, editors , *Phase Diagrams for Ceramists* (American Ceramic Society, Columbus, OH, 1964).
[67] J. M. Ferry and J. G. Blencoe, Am. Mineral. **63**, 1225 (1978).
[68] G. Shirane, R. E. Newnham, and R. Pepinsky, Phys. Rev. **96**, 581 (1954).
[69] M. Ahtee and A. W. Hewat, Acta Crystallogr. Sect. A **34**, 309 (1978).
[70] M. Bäurer, S.-J. Shih, C. Bishop, M. P. Harmer, D. Cockayne, and M. J. Hoffmann, Acta Mater. **58**, 290 (2010).